PHYSICAL REVIEW E **82**, 016703 (2010)

Lattice-Boltzmann simulation of laser interaction with weakly ionized helium plasmas

Huayu Li
Department of Mechanical Engineering, Michigan State University, East Lansing, Michigan 48824-1226, USA

Hyungson Ki*
School of Mechanical and Advanced Materials Engineering, Ulsan National Institute of Science and Technology, Ulsan, South Korea

(Received 9 August 2009; revised manuscript received 2 April 2010; published 14 July 2010)

This paper presents a lattice Boltzmann method for laser interaction with weakly ionized plasmas considering electron impact ionization and three-body recombination. To simulate with physical properties of plasmas, the authors' previous work on the rescaling of variables is employed and the electromagnetic fields are calculated from the Maxwell equations by using the finite-difference time-domain method. To calculate temperature fields, energy equations are derived separately from the Boltzmann equations. In this way, we attempt to solve the full governing equations for plasma dynamics. With the developed model, the continuous-wave CO_2 laser interaction with helium is simulated successfully.

DOI: 10.1103/PhysRevE.82.016703 PACS number(s): 02.70.−c, 52.65.−y, 52.38.−r

I. INTRODUCTION

Laser plasma interaction (LPI) is becoming more and more important as it finds novel and critical applications, such as initiation of nuclear fusion, laser plasma accelerator [1], laser induced breakdown spectroscopy (LIBS) [2], and medical imaging based on laser-plasma generated x-rays [3,4]. In addition, laser plasma interaction can be found in some laser based manufacturing processes, such as laser welding [5].

LPI exhibits very complicated physical phenomena, and computational studies have been a primary mode of research. A wide variety of computational methods have been developed to study LPI, and currently two classes of methods seem to be most popular: macroscopic methods based on hydrodynamic models and microscopic methods based on the dynamics of charged particles. Hydrodynamic models offer a well-established set of governing equations and numerical methods, but they treat plasmas as continuum fluids using the continuum hypothesis. Therefore, a lot of physics can be lost during derivation procedures and hydrodynamic models are in some cases oversimplified. On the other hand, microscopic methods are direct implementations of microscopic behaviors of particle species. Among others, the particle-in-cell (PIC) method [6] is arguably the most popular method for plasma modeling. Theoretically, PIC can retain physics to the maximum extent, but it is computationally expensive and limited to relatively small physical domains.

In between the two classes of methods are mesoscopic methods based on the Boltzmann transport equation. The advantages of the Boltzmann equation lie in the fact that, it contains deeper information on the plasma system than macroscopic equation approaches while it is computationally more efficient than the microscopic approaches, such as PIC. In fact, theoretically, the Boltzmann equation, when solved with Maxwell's equations, gives exact solutions to plasma problems.

In this paper, we present a numerical method for LPI based on the lattice Boltzmann method (LBM). Although the LBM is developed independently of the Boltzmann equation, it has been shown that the lattice Boltzmann equation can be derived from the Boltzmann equation by discretization in both time and phase space [7]. Theoretically, the higher the order of the phase-space discretization is, the closer the solution of the LBM approaches to the actual solution of the Boltzmann transport equation; that is, more information can be recovered from the LBM. In this study, however, because the objective is to explore the possibility of the LBM for LPI simulation, a simple D2Q9 scheme is adopted. Therefore, as reported in [8], the present LBM is not expected to recover physics beyond the continuum limit. This study assumes that the plasma is weakly ionized, so only collisions with neutrals are modeled using the Bhatnagar-Gross-Brook (BGK) approximation [9], which is the inherent collision algorithm in the LBM. For the sake of simplicity, only electron impact ionization and three-body recombination are considered for inelastic collision processes. Electromagnetic fields are calculated from the Maxwell equations using the finite-difference time-domain (FDTD) method [10]. The Maxwell equations and the lattice Boltzmann equations are coupled by the external force and current density. By using the standard D2Q9 algorithm in this study, only number densities and velocities can be calculated from the LBM. Thus, in order to calculate temperature fields, a separate set of energy equations is derived and included in this model. This method is applied to continuous-wave CO_2 laser interaction with helium plasmas, and some interesting results are presented.

II. MATHEMATICAL MODEL

A. Lattice Boltzmann equations

In this study, the following assumptions are used to simplify the model:

(1) The helium plasma is weakly ionized, so only the collisions with neutral particles are considered.

(2) Only first ionization is considered. Therefore, the plasma is composed of electrons, neutrals, and singly ionized helium atoms.

*Corresponding author. hski@unist.ac.kr

(3) Only electron impact ionization and three-body recombination are considered. Other inelastic collisions, such as excitation, de-excitation, and charge attachment are neglected.

Based upon the assumptions above, the Boltzmann equations with BGK collision terms for electrons, ions, and neutrals can be written as [11,12]

$$\frac{\partial f_e}{\partial t} + \mathbf{v}_e \cdot \nabla f_e + \mathbf{a}_e \cdot \nabla_{\mathbf{v}_e} f_e = -\frac{f_e - f_{en}^{eq}}{\lambda_{en}} + R_e f_e^{eq}, \quad (1)$$

$$\frac{\partial f_i}{\partial t} + \mathbf{v}_i \cdot \nabla f_i + \mathbf{a}_i \cdot \nabla_{\mathbf{v}_i} f_i = -\frac{f_i - f_{in}^{eq}}{\lambda_{in}} + R_i f_i^{eq}, \quad (2)$$

$$\frac{\partial f_n}{\partial t} + \mathbf{v}_n \cdot \nabla f_n = -\frac{f_n - f_{nn}^{eq}}{\lambda_{nn}} - R_n f_n^{eq}, \quad (3)$$

where the subscript s $(s=e,i,n)$ denotes the type of particles and can take e, i, and n for electrons, ions and neutrals, respectively; $f_s(\mathbf{x},\mathbf{v}_s,t)$ is the single particle distribution function of particle species s; $\mathbf{v}_s$ is its microscopic velocity; λ_{en}, λ_{in}, λ_{nn} are the relaxation times for electron-neutral, ion-neutral, and neutral-neutral collisions, respectively; f_{en}^{eq}, f_{in}^{eq}, f_{nn}^{eq} are the equilibrium distribution functions of electrons, ions, neutrals, respectively, due to the collisions with neutrals; R_s is the coefficient for ionization and recombination; $\mathbf{a}_s$ is the acceleration due to the Lorentz force and it is $\mathbf{a}_s = q_s(\mathbf{E}+\mathbf{v}_s \times \mathbf{B})/m_s$, where q_s and m_s are the charge and molecular mass of particle species s, respectively, $\mathbf{E}$ is the electric field, and $\mathbf{B}$ is the magnetic flux density.

If He *et al.*'s method [13] is used to approximate the external force terms, the following equations are obtained:

$$\frac{\partial f_e}{\partial t} + \mathbf{v}_e \cdot \nabla f_e = -\frac{f_e - f_{en}^{eq}}{\lambda_{en}} + \frac{\mathbf{a}_e \cdot (\mathbf{v}_e - \mathbf{u}_e)}{\theta_e^2} f_e^{eq} + R_e f_e^{eq}, \quad (4)$$

$$\frac{\partial f_i}{\partial t} + \mathbf{v}_i \cdot \nabla f_i = -\frac{f_i - f_{in}^{eq}}{\lambda_{in}} + \frac{\mathbf{a}_i \cdot (\mathbf{v}_i - \mathbf{u}_i)}{\theta_i^2} f_i^{eq} + R_i f_i^{eq}, \quad (5)$$

$$\frac{\partial f_n}{\partial t} + \mathbf{v}_n \cdot \nabla f_n = -\frac{f_n - f_n^{eq}}{\lambda_{nn}} - R_n f_n^{eq}. \quad (6)$$

The equilibrium distribution of species s due to self-collisions takes the following Maxwell-Boltzmann distribution,

$$f_s^{eq} = \frac{n_s}{2\pi\theta_s^2} \exp\left[-\frac{(\mathbf{v}_s - \mathbf{u}_s)^2}{2\theta_s^2} \right], \quad (7)$$

where n_s and $\mathbf{u}_s$ are the number density and macroscopic velocity of species s, respectively; $\theta_s = \sqrt{k_B T_s / m_s}$ is the sound speed, where k_B is the Boltzmann constant and T_s is the temperature of species s. From the kinetic theory [14], the relaxation time $\lambda_{ss'}$ is

$$\lambda_{ss'} = \frac{1}{\sigma_{ss'} n_{s'} \langle v_s \rangle} \quad (8)$$

where $\sigma_{ss'}$ is the cross section of the elastic collision between particle species s and s' and can be calculated as $\sigma_{ss'} = \pi(r_s + r_{s'})^2$, where r_s and $r_{s'}$ are the radii of particle species s and s', respectively; $n_{s'}$ is the number density of particle species s' and $\langle v_s \rangle$ is the average value of the thermal speed of particle species s [14],

$$\langle v_s \rangle = \left[\frac{8}{\pi} \frac{k_B T_s}{m_s} \right]^{1/2}. \quad (9)$$

Note that the sound speed of particles, the equilibrium distribution functions and the relaxation times are not only dependent on the particle number densities, but also on the particle temperatures in the present model.

In this study, unlike the author's previous work [11] the cross-collision equilibrium distribution function f_{en}^{eq} is defined as

$$f_{en}^{eq} = \frac{n_e}{2\pi\theta_{en}^2} \exp\left[-\frac{(\mathbf{v}_e - \mathbf{u}_{en})^2}{2\theta_{en}^2} \right], \quad (10)$$

where $\mathbf{u}_{en}$ is the barycentric velocity of the binary collision between electrons and neutrals,

$$\mathbf{u}_{en} = \frac{\rho_e \mathbf{u}_e + \rho_n \mathbf{u}_n}{\rho_e + \rho_n} \quad (11)$$

and sound speed θ_{en} is defined as

$$\theta_{en} = \sqrt{\frac{k_B T_{en}}{m_e}}, \quad (12)$$

where T_{en} is the electron temperature after elastic collisions with neutrals in the time period of λ_{en}. From the kinetic theory [14] and considering the ionization and recombination process, T_{en} can be found as

$$T_{en} = T_e + \frac{2m_{en}(T_n - T_e)}{m_e + m_n} + \frac{m_n m_{en}(\mathbf{u}_n - \mathbf{u}_e)^2}{3k_B(m_e + m_n)} - \frac{2\lambda_{en} R_e U_i e}{3k_B}, \quad (13)$$

where $m_{en} = \frac{m_e m_n}{m_e + m_n}$ is the reduced mass of electron and neutral, U_i is the first ionization potential (for helium, $U_i = 24.59$ eV) and e is the unit electronic charge ($1e = 1.6 \times 10^{-19} c$). T_{en} is used here because, to correctly describe the ionization and recombination dynamics, it is necessary to describe the postcollision states of the particles. Mathematically, the adoption of T_{en} in the equilibrium distribution function describes the energy transfer between electrons and neutrals due to the collisions. Similarly, the cross-collision equilibrium distribution function f_{in}^{eq} has the following definition,

$$f_{in}^{eq} = \frac{n_i}{2\pi\theta_{in}^2} \exp\left[-\frac{(\mathbf{v}_i - \mathbf{u}_{in})^2}{2\theta_{in}^2} \right], \quad (14)$$

where $\theta_{in} = \sqrt{\frac{k_B T_{in}}{m_i}}$ and T_{in} is calculated as

$$T_{in} = T_i + \frac{2m_{in}(T_n - T_i)}{m_i + m_n} + \frac{m_n m_{in}(\mathbf{u}_n - \mathbf{u}_i)^2}{3k_B(m_i + m_n)}, \quad (15)$$

where the reduced mass of ions and neutrals is $m_{in} = \frac{m_i m_n}{m_i + m_n}$. Note that there is no ionization term in the above equation.

The last terms in Eqs. (4)–(6) represent the rates of change of the particle distribution functions due to ionization of neutral particles and recombination of charged particles. In this model, only electron impact ionization and three-body recombination are considered. Then the ionization and recombination (IR) coefficient for electrons can be decomposed into the ionization part and recombination part:

$$R_e = R_e^i - R_e^r \tag{16}$$

where R_e^i and R_e^r represent the electron impact ionization rate and the recombination rate, respectively. The electron impact ionization rate can be expressed as

$$R_e^i = \sigma_i n_n \langle v_e \rangle, \tag{17}$$

where $\langle v_e \rangle$ is the average value of the thermal speed of electrons and can be evaluated from Eq. (9); σ_i is the cross section of electron impact ionization which is dependent on the electron energy $m_e \mathbf{v}_e^2/2$. The data of σ_i for helium as a function of electron energy can be found in literature [15–17]. For the three-body recombination, the formula in [18] is adopted in this study,

$$R_e^r = \frac{0.822 \times 10^{-33}}{T_e^{4.5}} n_e n_i, \tag{18}$$

where the electron temperature T_e is in the units of eV. Once R_e is calculated by Eqs. (17) and (18), the IR coefficients of ions and neutrals can be calculated as $R_i = \frac{n_e}{n_i} R_e$ and $R_n = \frac{n_e}{n_n} R_e$, respectively.

B. Energy equations and Maxwell equations

In this study, the standard D2Q9 lattice is employed. Hence, a separate set of energy equations for three species must be introduced. Starting with the Boltzmann equation, the corresponding energy equation can be obtained by taking velocity moments of the distribution functions with respect to the microscopic velocity. Multiplying $\chi(\mathbf{v}_e) = \frac{1}{2} m_e \mathbf{v}_e^2$ on every term in Eq. (4) and integrating each term with respect to $\mathbf{v}_e$ from the negative infinity to positive infinity, we can obtain

$$\int_{\mathbf{v}} \chi(\mathbf{v}_e) \frac{\partial f_e}{\partial t} d\mathbf{v}_e + \int_{\mathbf{v}} \chi(\mathbf{v}_e) \mathbf{v}_e \cdot \nabla f_e d\mathbf{v}_e = -\frac{1}{\lambda_{en}} \int_{\mathbf{v}} \chi(\mathbf{v}_e)(f_e - f_{en}^{eq}) d\mathbf{v}_e + R_e \int_{\mathbf{v}} \chi(\mathbf{v}_e) f_e^{eq} d\mathbf{v}_e + \frac{\mathbf{a}_e}{\theta_e^2} \cdot \int_{\mathbf{v}} \chi(\mathbf{v}_e)(\mathbf{v}_e - \mathbf{u}_e) f_e^{eq} d\mathbf{v}_e. \tag{19}$$

Following the similar derivation procedure in [19], we can obtain the energy equation for electrons as

$$\frac{\partial \varepsilon_e}{\partial t} + \nabla \cdot (\varepsilon_e \mathbf{u}_e) = -\nabla \cdot (\mathbf{P}_e \cdot \mathbf{u}_e) + \nabla \cdot (\kappa_e \nabla T_e) + \mathbf{J}_e \cdot \mathbf{E} - \frac{3 k_B n_e m_{en} (T_e - T_n)}{\lambda_{en}(m_e + m_n)} + \frac{m_e n_e}{\lambda_{en}} \mathbf{u}_{en} \cdot (\mathbf{u}_{en} - \mathbf{u}_e) - R_e n_e U_i e + R_e \varepsilon_e \tag{20}$$

where $\varepsilon_e = \frac{3}{2} n_e k_B T_e + \frac{1}{2} m_e n_e \mathbf{u}_e^2$ is the total energy of electrons; $-\kappa_e \nabla T_e = \mathbf{q}_e$ is the electron heat flux where $\kappa_e = \frac{1}{2} n_e k_B \langle v_e \rangle \lambda_{en}$ is the electron thermal conductivity; $\mathbf{J}_e = -e n_e \mathbf{u}_e$ is the electron current density and $\mathbf{J}_e \cdot \mathbf{E}$ is the Joule heating term for electrons which can be interpreted as the energy absorbed from the incident laser beam. The fourth term on the right hand side of Eq. (20), which is obtained by substituting T_{en} [Eq. (13)] into the energy equation, represents the energy transfer between electrons and neutrals due to the cross collisions. The fifth term describes the kinetic energy change of electron due to collisions while the sixth term is the energy loss of electrons because of the ionization and the last term represents the total energy change of electrons due to the ionization. Similarly, the energy equations for ions and neutrals are

$$\frac{\partial \varepsilon_i}{\partial t} + \nabla \cdot (\varepsilon_i \mathbf{u}_i) = -\nabla \cdot (\mathbf{P}_i \cdot \mathbf{u}_i) + \nabla \cdot (\kappa_i \nabla T_i) + \mathbf{J}_i \cdot \mathbf{E} - \frac{3 k_B n_i m_{in} (T_i - T_n)}{\lambda_{in}(m_i + m_n)} + \frac{m_i n_n}{\lambda_{in}} \mathbf{u}_{in} \cdot (\mathbf{u}_{in} - \mathbf{u}_i) + R_i \varepsilon_i \tag{21}$$

and

$$\frac{\partial \varepsilon_n}{\partial t} + \nabla \cdot (\varepsilon_n \mathbf{u}_n) = -\nabla \cdot (\mathbf{P}_n \cdot \mathbf{u}_n) + \nabla \cdot (\kappa_n \nabla T_e) + \frac{3 k_B n_e m_{en} (T_e - T_n)}{\lambda_{en}(m_e + m_n)} + \frac{m_n n_e}{\lambda_{en}} \mathbf{u}_{en} \cdot (\mathbf{u}_{en} - \mathbf{u}_n) + \frac{3 k_B n_i m_{in} (T_i - T_n)}{\lambda_{in}(m_i + m_n)} + \frac{m_n n_i}{\lambda_{in}} \mathbf{u}_{in} \cdot (\mathbf{u}_{in} - \mathbf{u}_n) + R_n \varepsilon_n \tag{22}$$

Equations (20)–(22) constitute a full set of the energy equations for the three species in a weakly ionized plasma. When solved with the lattice Boltzmann equations, temperature fields can be obtained. In this study, Eqs. (20)–(22) are solved by a finite volume method.

To obtain electromagnetic fields, the Maxwell equations are solved in this study. In this way, the Lorentz force terms in the Boltzmann equations and the Joule heating terms in the energy equations can be calculated. In this study, the finite-difference time-domain (FDTD) method [10] is adopted to solve the two curl equations,

$$\nabla \times \mathbf{H} = \varepsilon \frac{\partial \mathbf{E}}{\partial t} + \mathbf{J}, \tag{23}$$

$$\nabla \times \mathbf{E} = -\mu \frac{\partial \mathbf{H}}{\partial t}, \tag{24}$$

where $\mathbf{E}$ and $\mathbf{H}$ are the electric and magnetic field, respectively; ε and μ are the permittivity and magnetic permeability, and $\mathbf{J}$ is the current density which can be calculated as

$$\mathbf{J} = e(n_i \mathbf{u}_i - n_e \mathbf{u}_e) \tag{25}$$

Here, the number densities and velocities of electrons and ions are obtained from the lattice Boltzmann calculation. Note that the two divergence equations are automatically satisfied by the Yee lattice grid [10] used by the FDTD. The UPML (uniaxial perfectly matched layer) boundary condition [10] is used to terminate the computational domain.

C. Rescaling scheme

In this study, to correctly simulate with physical properties of plasmas, the author's method presented in [20] is employed. Considering the fact that the lattice Boltzmann equation is a convection-diffusion equation, the rescaling method is based on the following two rules: (1) the physical viscosity is equal to the lattice viscosity (the viscosity recovered from the LBM) and (2) the characteristic flow velocity due to the external force should not be altered by the scheme. (In the following discussion, the variables with a tilde represent the lattice variables, i.e., the quantities derived from the LBM. Also, we will consider electrons for derivation for the sake of simplicity.)

From the first rule, equating the lattice viscosity

$$\tilde{\nu} = (\tau - 0.5)\tilde{\theta}^2 \Delta t = \frac{(\tau - 0.5)\tilde{\theta}\Delta x}{\sqrt{3}} \tag{26}$$

with the physical viscosity

$$\nu = \frac{8\theta^2 \lambda}{3\pi} \tag{27}$$

yields

$$\tilde{\theta} = \sqrt{\frac{8\lambda}{3\pi \Delta t(\tau - 0.5)}}\theta. \tag{28}$$

Here, $\Delta x = \sqrt{3}\tilde{\theta}\Delta t$ and $\tilde{\theta}$ is the lattice sound speed. The above equation can be rewritten as

$$\tilde{\theta} = \frac{\theta}{\gamma} \tag{29}$$

if the rescaling parameter γ is defined as follows:

$$\gamma = \sqrt{\frac{3\pi \Delta t(\tau - 0.5)}{8\lambda}}. \tag{30}$$

Here, λ and τ are the physical relaxation time and the dimensionless relaxation time for collisions, respectively.

As for the rescaling of the acceleration term, we define the characteristic velocity in this model as the drift velocity of the charged particles caused by the Lorentz force; that is, $\mathbf{U}_0 = \mathbf{a}\lambda$. According to the second rescaling rule, the lattice acceleration term can be found as [20]

$$\tilde{\mathbf{a}} = \frac{\lambda}{\tilde{\lambda}}\mathbf{a}, \tag{31}$$

where $\tilde{\lambda}$ is the lattice relaxation time which can be found directly from the relationship of $\tilde{\lambda} = \tau \Delta t$. In the above equations, the dimensionless relaxation time τ is a selected constant between 0.5 and 3.0 and is identical for all the three species of particles in the simulation.

Note that because the time step in this study is constrained by the stability requirement of the FDTD method, a slightly different procedure of selecting parameters is used. In [20], two parameters, τ and Δx, are chosen freely before the selection of other lattice parameters, and all three dimensionless relaxation times are set to 0.9. Once the lattice sound speed is determined from the rescaling rules, time step is calculated as $\Delta t = \Delta x / \sqrt{3}\tilde{\theta}$. However, in the current simulation, the time step Δt must meet the stability requirement of the FDTD method, which means that Δt will be much smaller. (The procedure of selecting the time step will be explained in the next section.) In this study, therefore, the lattice size Δx is determined first by the resolution requirements of the problem. Here, Δx is chosen as 1/20 of the laser wavelength to capture the accurate wave like behaviors of the laser beam. Next, the time step is determined by the stability requirement of the FDTD method [Eq. (44)]. After selecting a dimensionless relaxation time in the value range between 0.5 and 3.0, the rescaling factor γ can be calculated from Eq. (30). Then the lattice sound speed $\tilde{\theta}$ can be found from Eq. (29), the lattice relaxation time $\tilde{\lambda}$ is obtained from the relationship of $\tilde{\lambda} = \tau \Delta t$, and the lattice acceleration term can be obtained from Eq. (31).

D. Lattice Boltzmann method

Once parameters are rescaled, the traditional D2Q9 [21] scheme can be used to solve the lattice Boltzmann equations. In this scheme, the velocity is discretized into nine discrete velocity components,

$$\mathbf{e}_s^\alpha = \begin{cases} (0,0) & \alpha = 0 \\ \sqrt{3}(\cos\varphi^\alpha, \sin\varphi^\alpha)\tilde{\theta}_s & \alpha = 1,2,3,4 \\ \sqrt{6}(\cos\varphi^\alpha, \sin\varphi^\alpha)\tilde{\theta}_s & \alpha = 5,6,7,8, \end{cases} \tag{32}$$

where the superscript α denotes the αth component in the phase space; $\mathbf{e}_s^\alpha$ is the αth component of the discretized microscopic velocity of particle species s and φ^α takes the following form:

$$\begin{cases} \varphi^\alpha = (\alpha - 1)\pi/2 & \alpha = 1,2,3,4 \\ \varphi^\alpha = (\alpha - 5)\pi/2 + \pi/4 & \alpha = 5,6,7,8. \end{cases} \tag{33}$$

Then the self-collision equilibrium distribution function can be expressed as

$$f_s^{\alpha,eq} = \omega_\alpha n_s \left\{ 1 + \frac{(\mathbf{e}_s^\alpha \cdot \mathbf{u}_s)}{\tilde{\theta}_s^2} + \frac{(\mathbf{e}_s^\alpha \cdot \mathbf{u}_s)^2}{2\tilde{\theta}_s^4} - \frac{\mathbf{u}_s^2}{2\tilde{\theta}_s^2} \right\}. \tag{34}$$

And the cross-collision equilibrium distribution functions are

$$f_{en}^{\alpha,eq} = \omega_\alpha n_e \left\{ 1 + \frac{(\mathbf{e}_e^\alpha \cdot \mathbf{u}_{en})}{\tilde{\theta}_{en}^2} + \frac{(\mathbf{e}_e^\alpha \cdot \mathbf{u}_{en})^2}{2\tilde{\theta}_{en}^4} - \frac{\mathbf{u}_{en}^2}{2\tilde{\theta}_{en}^2} \right\} \tag{35}$$

and

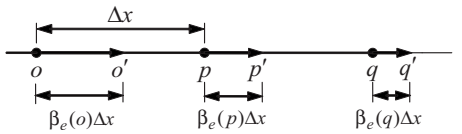

FIG. 1. Schematic of the interpolation scheme. The value of distribution function at p can be found by using the postcollision values at o', p', and q'.

$$f_{in}^{\alpha,eq} = \omega_\alpha n_i \left\{ 1 + \frac{(\mathbf{e}_i^\alpha \cdot \mathbf{u}_{in})}{\tilde{\theta}_{in}^2} + \frac{(\mathbf{e}_i^\alpha \cdot \mathbf{u}_{in})^2}{2\tilde{\theta}_{in}^4} - \frac{\mathbf{u}_{in}^2}{2\tilde{\theta}_{in}^2} \right\} \quad (36)$$

where the coefficient ω_α is

$$\omega_\alpha = \begin{cases} 4/9 & \alpha = 0 \\ 1/9 & \alpha = 1,2,3,4 \\ 1/36 & \alpha = 5,6,7,8. \end{cases} \quad (37)$$

Finally, the lattice Boltzmann equations derived from the Boltzmann equations [Eqs. (4)–(6)] can be written as

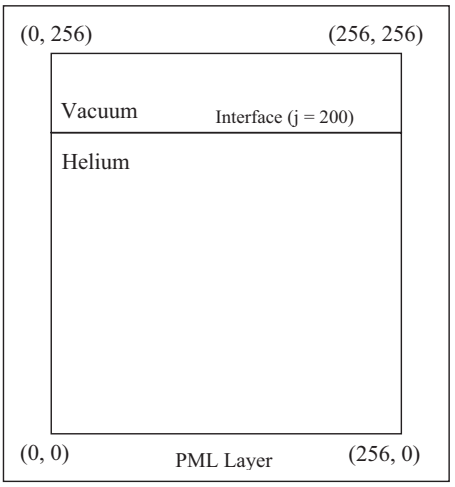

FIG. 2. Schematic of the computational domain with the grid information and the UPML for the FDTD solver.

$$f_e^\alpha(\mathbf{x} + \mathbf{e}_e^\alpha \Delta t, t + \Delta t) = f_e^\alpha(\mathbf{x},t) - \frac{f_e^\alpha(\mathbf{x},t) - f_{en}^{\alpha,eq}(\mathbf{x},t)}{\tau_{en}} + \Delta t J_e^\alpha(\mathbf{x},t) + \Delta t F_e^\alpha(\mathbf{x},t), \quad (38)$$

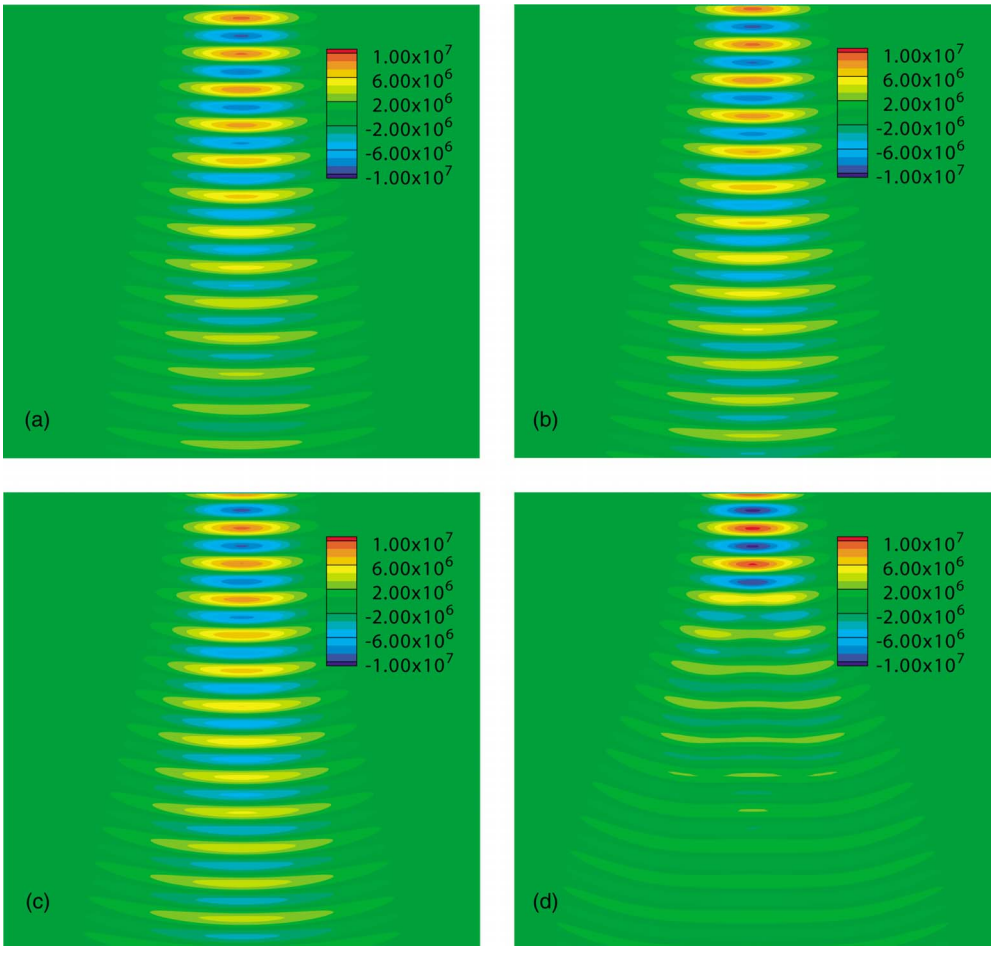

FIG. 3. (Color online) x-component electric field (domain size: 135.68×135.68 μm^2). (a) $t=5$ ps, (b) $t=15$ ps, (c) $t=40$ ps, and (d) $t=120$ ps.

$$f_i^\alpha(\mathbf{x}+\mathbf{e}_i^\alpha\Delta t,t+\Delta t)=f_i^\alpha(\mathbf{x},t)-\frac{f_i^\alpha(\mathbf{x},t)-f_{in}^{\alpha,eq}(\mathbf{x},t)}{\tau_{in}}+\Delta tJ_i^\alpha(\mathbf{x},t)+\Delta tF_i^\alpha(\mathbf{x},t), \quad (39)$$

$$f_n^\alpha(\mathbf{x}+\mathbf{e}_n^\alpha\Delta t,t+\Delta t)=f_n^\alpha(\mathbf{x},t)-\frac{f_n^\alpha(\mathbf{x},t)-f_n^{\alpha,eq}(\mathbf{x},t)}{\tau_{nn}}-\Delta tJ_n^\alpha(\mathbf{x},t), \quad (40)$$

where τ_{sn} is the dimensionless relaxation time for collisions between particles s and n; $J_s^\alpha=R_sf_s^{\alpha,eq}(\mathbf{x},t)$ is the gain/loss term of species s due to ionization and recombination; and $F_{e(i)}^\alpha(\mathbf{x},t)=\frac{\tilde{\mathbf{a}}_{e(i)}\cdot(\mathbf{e}_{e(i)}^\alpha-\mathbf{u}_{e(i)})}{\tilde{\theta}_{e(i)}^2}f_{e(i)}^{\alpha,eq}(\mathbf{x},t)$ is the external force term for charged particles. The above equations can be solved by the collision and streaming scheme on the D2Q9 lattice. Then the macroscopic variables can be calculated as

$$n_s(\mathbf{x},t)=\sum_\alpha f_e^\alpha(\mathbf{x},t), \quad (41)$$

$$n_s(\mathbf{x},t)\mathbf{u}_s(\mathbf{x},t)=\sum_\alpha \mathbf{e}_s^\alpha f_e^\alpha(\mathbf{x},t). \quad (42)$$

Since the present model is composed of three submodels, the time step should be selected as

$$\Delta t=\min(\Delta t_{LBM},\Delta t_{FDTD},\Delta t_{ENG}), \quad (43)$$

where Δt_{LBM} is the time step for the LBM, Δt_{FDTD} is the time step for the FDTD, $\Delta t_{FDTD}\leq\frac{\Delta x}{\delta c}$ (where c is the speed of light and δ is a constant greater than 1), and Δt_{ENG} is the time step for the energy equations. In this study, Δt_{FDTD} is the smallest, so we choose the time step as

$$\Delta t=\Delta t_{FDTD}=\frac{\Delta x}{\delta c}. \quad (44)$$

Since Δt_{LBM} is much larger than Δt_{FDTD}, particle species cannot stream to the adjacent node points during Δt_{FDTD}. Thus, an interpolation scheme needs to be introduced to find the on-node values of the distribution functions after the streaming step in LBM. Referring to Fig. 1, the following interpolation formula is obtained for electrons,

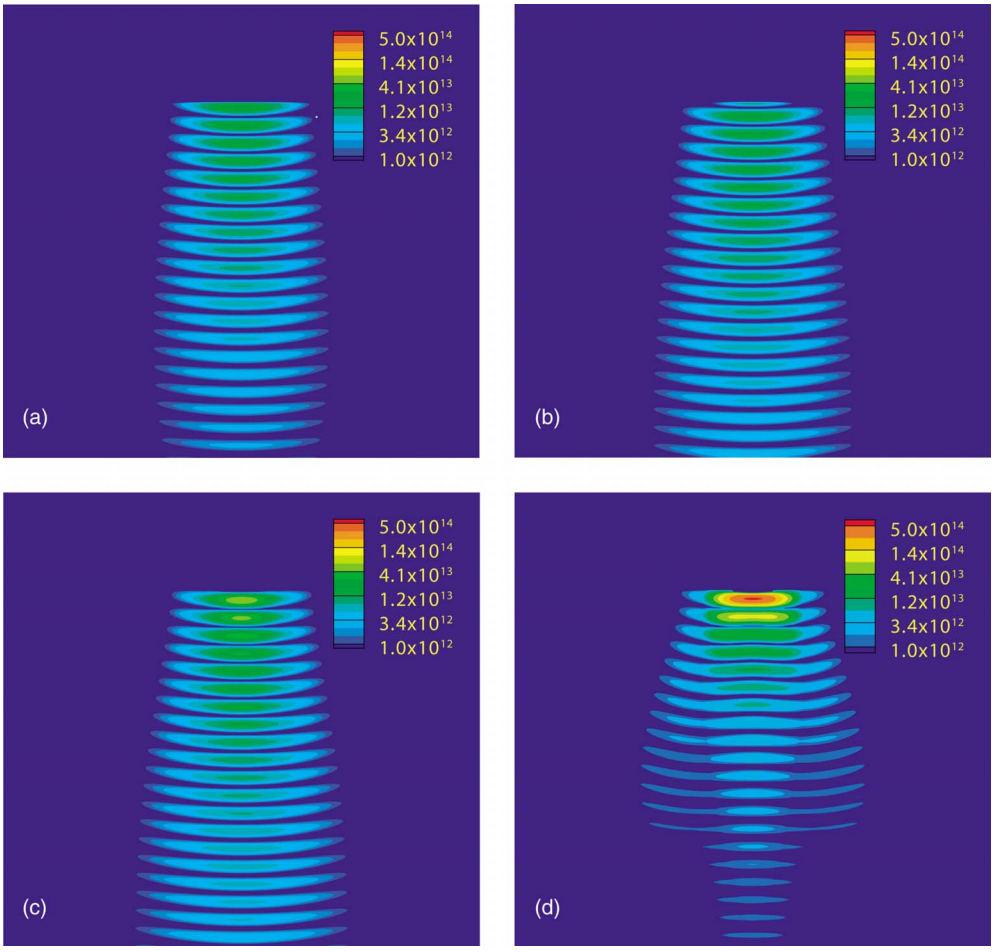

FIG. 4. (Color online) Joule heating patterns (domain size: 135.68×135.68 μm^2). (a) $t=5$ ps, (b) $t=15$ ps, (c) $t=40$ ps, and (d) $t=120$ ps

$$f_e(p) = \frac{nkf_e(p')}{(n-m)(k-m)} - \frac{mnf_e(o')}{(k-m)(n-k)} + \frac{kmf_e(q')}{(n-m)(n-k)}. \tag{45}$$

Here, $m=\beta_e(p)$, $n=\beta_e(q)+1$ and $k=\beta_e(o)-1$, and $\beta_e(\mathbf{x},t) = \sqrt{3}\tilde{\theta}_e(\mathbf{x},t)\Delta t/\Delta x$. The interpolation scheme applied in this study is similar to the one used in [11]. However, since the lattice sound speed $\tilde{\theta}_e$ is dependent on temperature (and consequently, dependent on both time and space), the present interpolation formula is different from the one used in [11]. Interpolation formulas for neutrals and ions can be obtained similarly.

III. RESULTS AND DISCUSSION

In this study, the continuous-wave CO_2 laser interaction with helium is simulated with the presented model. The computational domain is a 135.68 μm $\times$ 135.68 μm square, which is discretized by a uniform 256 $\times$ 256 grid. The no-gradient boundary condition is applied on all the boundaries enclosing the helium. As shown in Fig. 2, a uniaxial perfectly matched layer (UPML) boundary condition is used for the FDTD solver. The PML thickness is 30 grid points. A CO_2 laser beam whose wavelength is 10.6 μm is incident from the top of the computational domain and propagates along the negative y direction. Initially, the helium is assumed to have a 0.01% ionization degree. The initial number densities of neutrals, ions and electrons are 2.687×10^{19}, 2.687×10^{15}, and 2.687×10^{15} cm^{-3}, respectively. The initial temperatures of all three species are $T_{e0}=T_{i0}=T_{n0}=1.058$ eV according to the Saha equation.

Figure 3 shows the x component of the electric field for the laser intensity of 1.25×10^7 W/cm^2, from which we can visualize how the laser beam propagates and interacts with the helium. Initially, intensity attenuation along the beam propagation direction is small, but as the ionization process is getting established, more and more laser energy is absorbed in the thin helium layer at the helium-vacuum interface. As seen in the figure, at about 120 ps, almost entire laser beam is blocked by the free electrons, and only a small fraction of the laser beam penetrates inside. Figure 4 shows the corresponding Joule heating patterns in helium. Initially, heating is pretty uniform in the beam propagation direction, but as time elapses, the heating is concentrated in the small area at the helium-vacuum interface. This is another evidence of the ionization process and free electron production. Once the laser beam crosses the interface, it will heat up free electrons. As a result, the electron energy, including both the macroscopic kinetic energy and the thermal energy, will go up. If the electron energy is higher than the ionization potential of helium, free electrons will be generated through the electron impact ionization process.

Figure 5 presents the evolution of the maximum electron number density in the whole domain for several laser intensity values. Note that the values shown in the figure are normalized electron number densities with respect to the initial neutral number density. Therefore, they are the maximum ionization degree in the computational domain at the given instant. As clearly seen, the maximum number density increases with time and tends to saturate at some point. However, although relatively low laser intensity values are used (1.25×10^7–2×10^7 W/cm^2), the maximum ionization de-

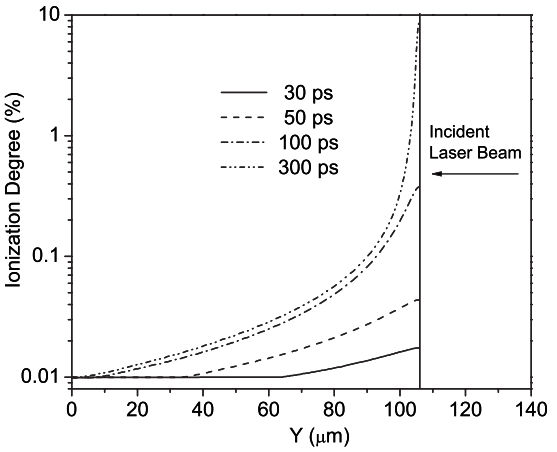

FIG. 6. Degree of ionization along the beam propagation axis.

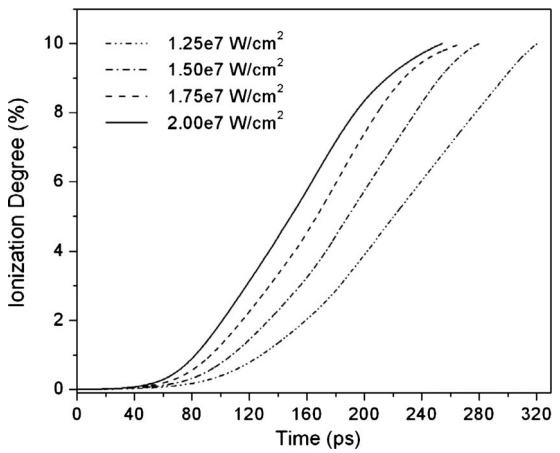

FIG. 5. Evolution of the maximum ionization degree in the domain.

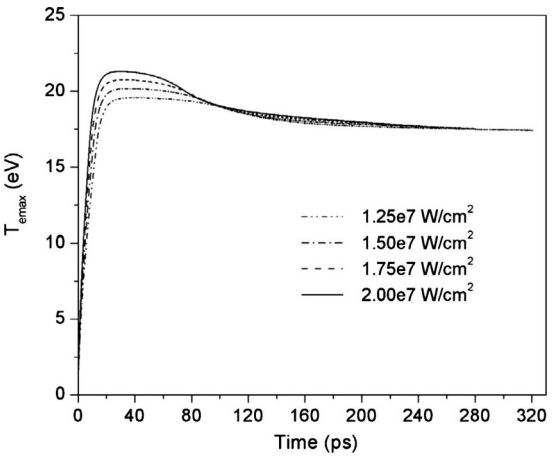

FIG. 7. Evolution of maximum electron temperature in the domain.

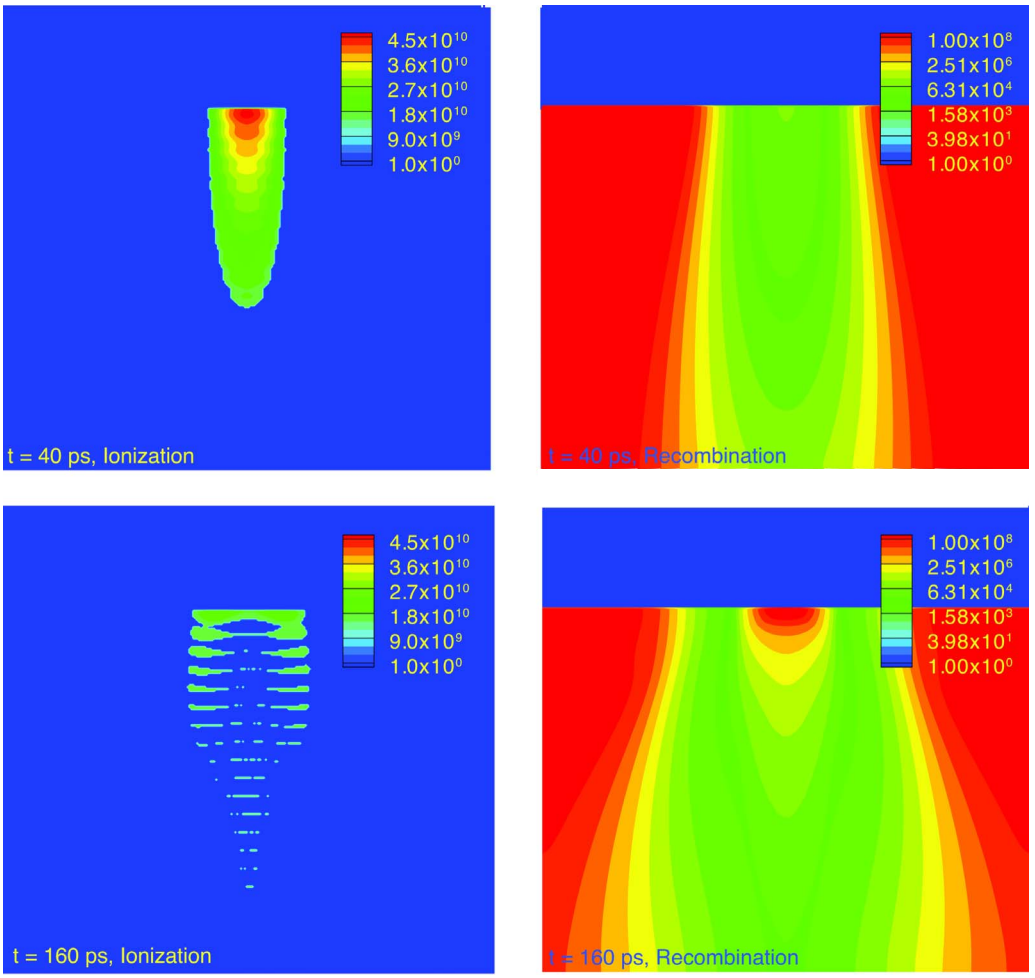

FIG. 8. (Color online) Ionization coefficient R_e^i (left) and Recombination coefficient R_e^r (right) (domain size: 135.68×135.68 μm^2).

gree becomes too large, about 10%, for all cases. This seems to be too large considering the small laser intensity values and violates the assumption of weakly ionized plasma. In reality, the maximum ionization degree occurs always at the very first grid point where the laser hits the helium along the centerline (let us call this point A), and after that point, it decreases very sharply. This is clearly shown in Fig. 6, which is the ionization degree distribution along the central line of the domain. The result is obtained for 1.25×10^7 W/cm^2. After 100 ps, the increase in the ionization degree in the whole domain is small except at a very small region near the interface: there is still a huge increase in the ionization degree there. However, the authors believe that this point is like a singularity due to the discontinuity in geometry (vacuum and helium) and that the actual maximum ionization degree is less than 3%. Also, in most part of the domain, the ionization degree is less than 0.5%, which justifies the assumption of weakly ionized plasma. Apparently, this high ionization degree is partially due to the recursion effect: more electrons induce higher energy absorption, which in turn increases the free electron production rate. Note that a logarithmic scale is used in Fig. 6.

In Fig. 5, we can also see that the electrons are generated with a higher rate if the laser intensity is higher. That is natural because higher laser intensity indicates that more laser energy is put into the domain in a unit time and thus leads to a quicker heating of the electrons. As long as the electron energy is greater than the ionization potential, the ionization will keep taking place and more and more free electrons will be generated. However, ionization itself is a cooling mechanism for electrons because in impact ionization the electron energy is used for ionization. This is apparent in the energy

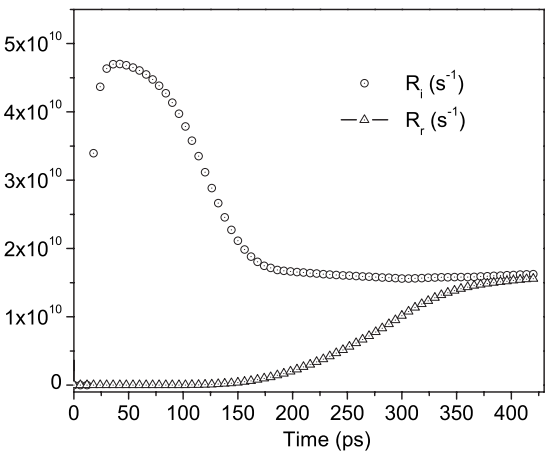

FIG. 9. Time history of ionization and recombination coefficients at point A for laser intensity of 1.25×10^7 W/cm^2.

equation where the ionization process appears as a sink term. Consequently, with more electrons generated, the electron temperature begins to decrease as shown in Fig. 7, which is the time history of maximum electron temperature in the computational domain. In this figure, comparing with Fig. 5, we can see that the electron temperature increases very quickly in a very short amount of time when the ionization has not taken place effectively. For example, at the laser intensity of 2×10^7 W/cm^2, the maximum electron number density starts to increase at around 38 ps, which corresponds to the point at which temperature starts to decrease.

As the electron temperature decreases, the ionization rate is reduced accordingly. At the same time, since the recombination rate is proportional to the number densities of charged particles and inversely proportional to the electron temperature, the recombination becomes more and more prominent. Reduction of ionization and enhancement of recombination lead to a lower generation rate of free electrons, and therefore, the electron number density saturates as shown in Fig. 5.

Figure 8 is the distributions of ionization coefficient R_e^i and recombination coefficient R_e^r at $t=40$ ps and $t=160$ ps for the laser intensity of 1.25×10^7 W/cm^2. Initially, the ionization coefficient is very high in the thin layer at the helium-vacuum interface while the recombination coefficient is small there. This leads to a strong ionization process. As time elapses, the recombination coefficient increases and eventually becomes in the same range as the ionization coefficient. This is shown well in Fig. 9, which presents the time histories of the ionization and recombination coefficients at point A. In that figure, the ionization coefficient increases steeply and then decreases and reaches a steady

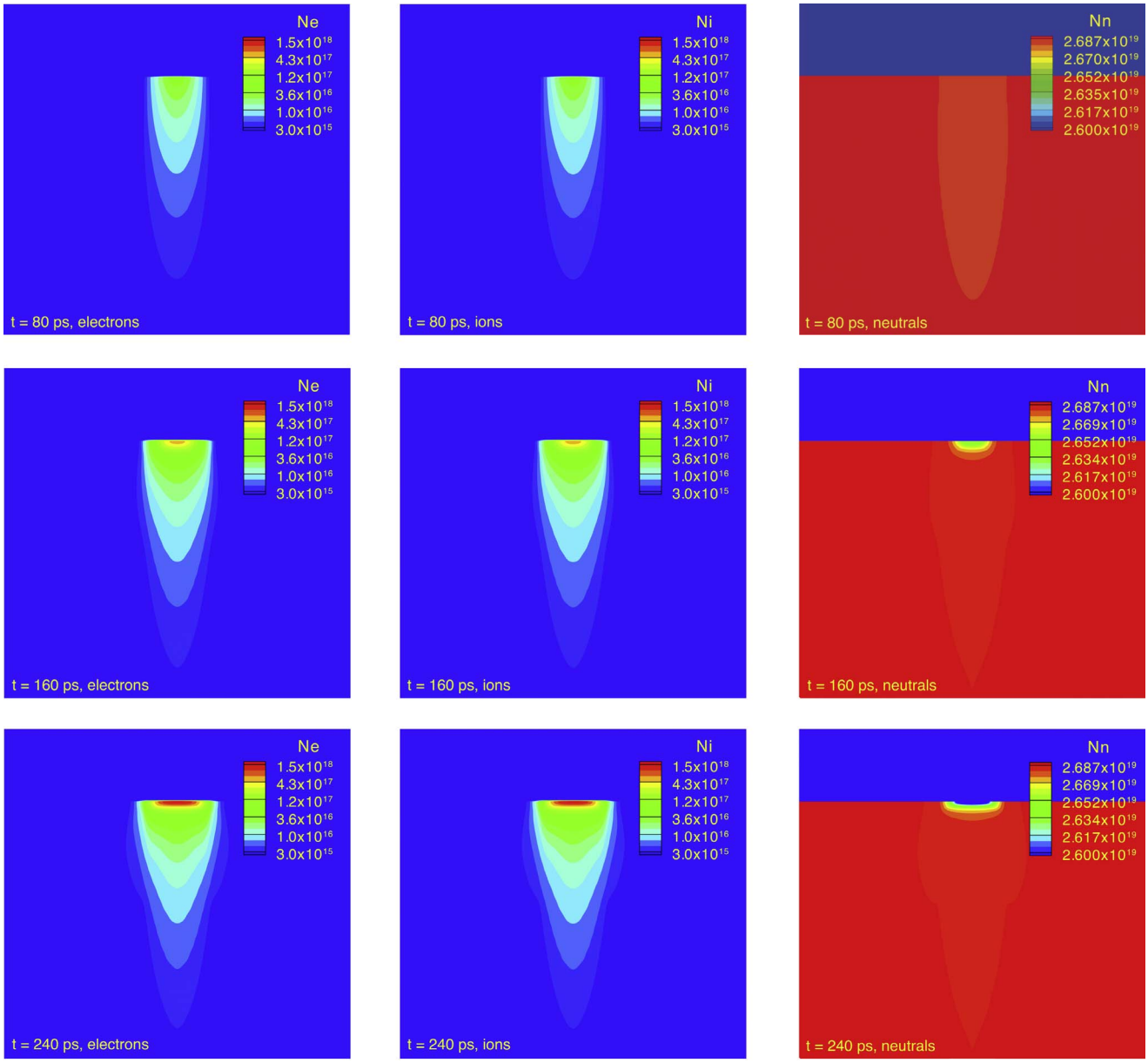

FIG. 10. (Color online) Snapshots of electron (left), ion (middle), and neutral (right) number densities (number of particles per cm^3) (domain size: 135.68×135.68 μm^2).

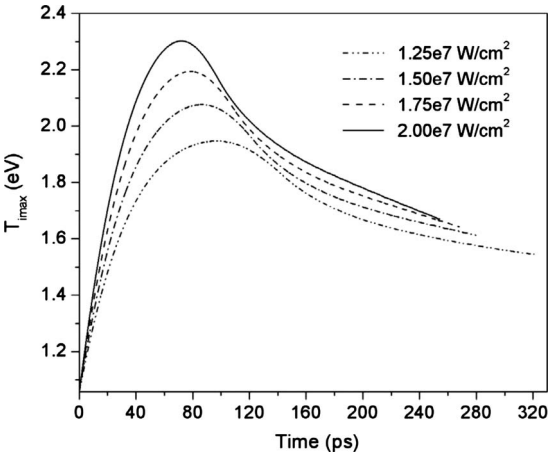

FIG. 11. Evolution of maximum ion temperature.

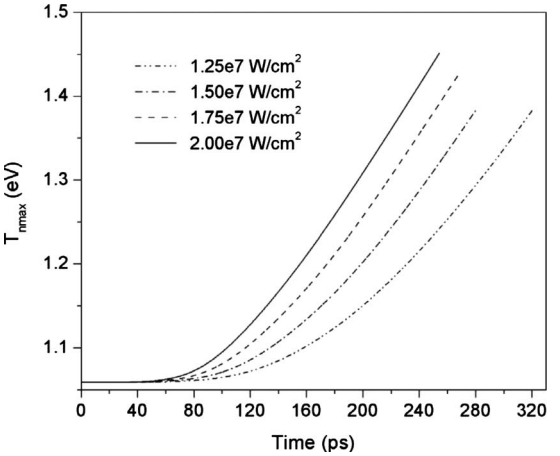

FIG. 12. Evolution of maximum neutral temperature.

state due to the decrease of the electron energy. As stated before, this energy loss is caused by the ionization itself because ionization is a cooling mechanism. Meanwhile, the recombination coefficient monotonically increases and reaches a steady state due to the combined effects of electron number density and temperature. Also, the recombination of charged particles releases energy, which can contribute to the increase in the electron temperature. Note that eventually the ionization and recombination coefficients converge to the same rate. One more thing to note in Fig. 9 is that the evolution of the ionization coefficient has the similar pattern as the evolution of electron temperature in Fig. 7. This is because the ionization coefficient is mainly dependent on the electron energy [Eq. (17)].

Figure 10 shows electron, ion and neutral number density distributions at 80, 160, and 240 ps for the laser intensity of 1.25×10^7 W/cm^2. The patterns of free electron and ion generation are very similar, which is reasonable because according to the model one electron from a neutral means the generation of one singly ionized ion at the same location. We

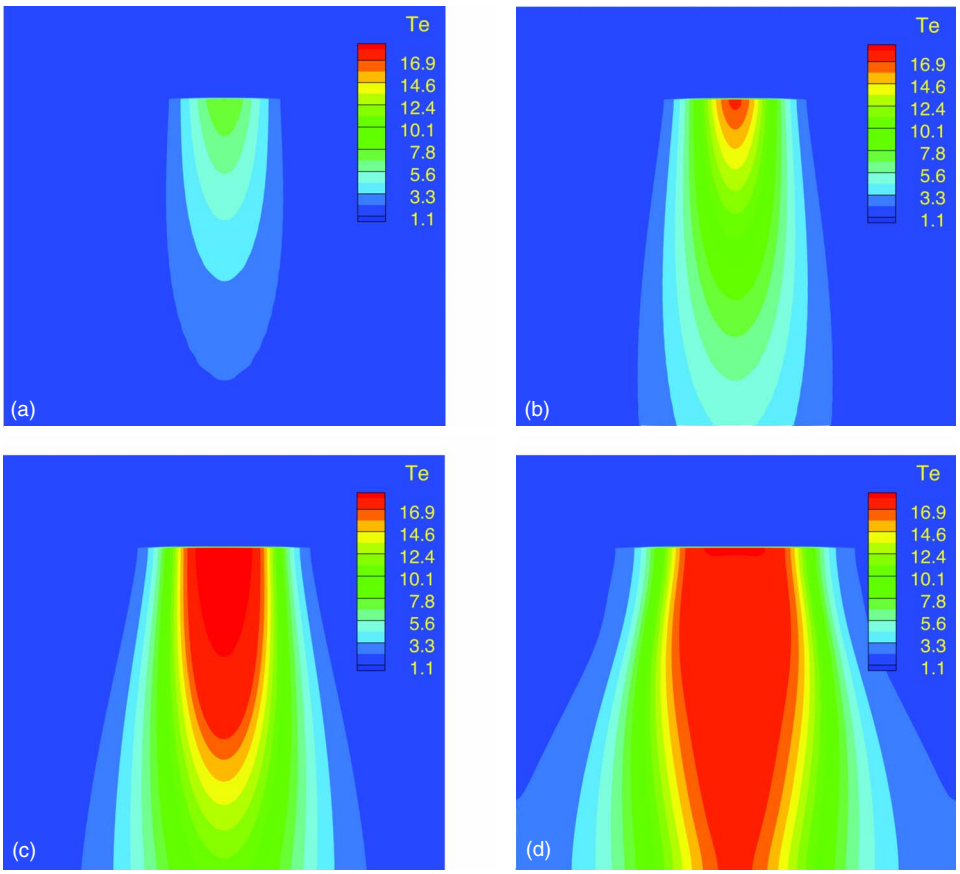

FIG. 13. (Color online) Electron temperature distributions (domain size: 135.68×135.68 μm^2). (a) $t=5$ ps, (b) $t=15$ ps, (c) $t=40$ ps, and (d) $t=120$ ps.

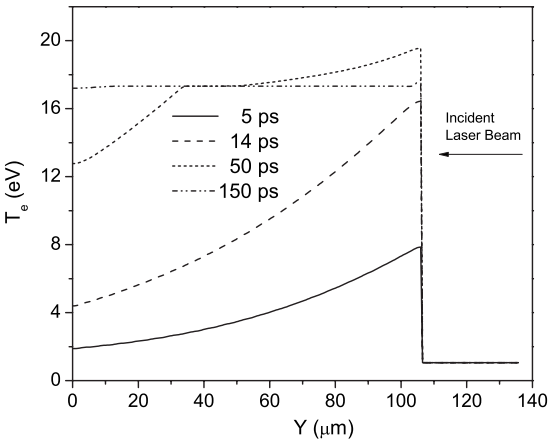

FIG. 14. Electron temperature distribution along the beam propagation axis.

can also see that the generation of free electrons and the loss of neutrals are matched well. Also, following the Gaussian laser distribution, more electrons are generated along the central line. It is also seen in Fig. 10 that most of the free electrons are generated in a thin layer at the helium-vacuum interface.

Figures 11 and 12 show the time histories of the maximum ion and neutral temperatures in the domain, respectively. The ions are directly heated by the laser, but the heating is much slower than the electron heating because the ions are much heavier than the electrons. The ion temperature also decreases after some time as do the electrons. However, the cause of this temperature decrease is primarily the attenuation of the electric field. That is why the ion temperature starts to decrease at a much later time than the electron temperature. Unlike the charged particles, neutrals are heated by the energy transferred from the charged particles. As long as there is temperature difference between charged particles and neutrals, the cross energy transfer will take place and the neutrals will continue to get heated.

Figure 13 presents the electron temperature distribution in the domain for 1.25×10^7 W/cm^2 at four intermediate times. Overall, the heated region expands spatially with time, and a very thin layer of intense heating along the helium-vacuum interface emerges with time. The heating in this layer is becoming more and more uniform. Also, we can observe that along the centerline temperature distribution becomes uniform too, which is clearly shown in Fig. 14. Figure 14 shows the electron temperature distributions at several intermediate times along the beam propagation axis. The incident laser intensity is 1.25×10^7 W/cm^2. It is shown that at about 150 ps, the temperature distribution becomes almost uniform at 17 eV.

Figure 15 shows the electric field, electron velocity field and ion velocity field at $t=5$ ps and $t=120$ ps. In the figure, the solid closed contours represent the streamlines of the vector fields. This plot shows the capabilities of the current model for capturing the dynamics of the particles. In the figures, the electrons move in a reverse direction relative to the electric field while the ions, which bear the positive charge, show a motion trace consistent with the electric field. As expected, the relative magnitude of the ion velocity, which is indicated in the figure by the length of the arrows, is much smaller than that of electrons.

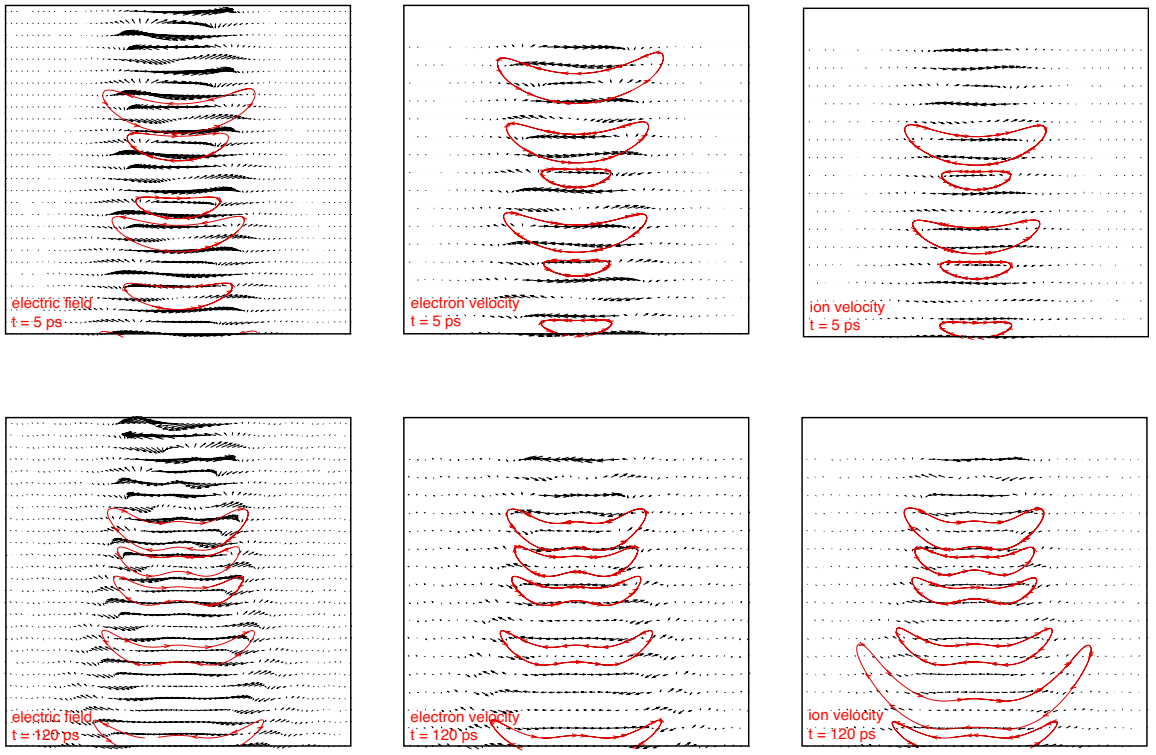

FIG. 15. (Color online) Electric field (left), electron velocity field (middle), and ion velocity field (right). Domain size: 135.68 $\times$135.68 μm^2. .

IV. CONCLUSION

In this paper, a lattice Boltzmann based numerical method for simulating LPI has been presented. To the best of the authors' knowledge, it is the first attempt to simulate LPI using the lattice Boltzmann method. In this method, the BGK approximation for the collisions with neutrals has been employed to model weakly ionized plasmas, and impact ionization and three-body recombination are considered for inelastic collision processes. The presented method has been applied to the continuous-wave CO_2 laser interaction with helium and the model was able to simulate complicated physical phenomena of LPI.

ACKNOWLEDGMENT

This research was partially supported by the research grant from the U.S. National Science Foundation (Grant No. 0425217) and the Basic Science Research Program through the National Research Foundation of Korea (NRF) funded by the Ministry of Education, Science and Technology (Grant No. 2010–0005744).

[1] V. Malka *et al.*, Nat. Phys. **4**, 447 (2008).
[2] C. Pasquini *et al.*, J. Braz. Chem. Soc. **18**, 463 (2007).
[3] C. Tillman *et al.*, J. Opt. Soc. Am. B **13**, 209 (1996).
[4] C. L. Gordon *et al.*, Opt. Lett. **20**, 1056 (1995).
[5] G. M. Petrov *et al.*, Phys. Rev. E **71**, 036411 (2005).
[6] R. W. Hockney and J. W. Eastwood, *Computer Simulation Using Particles* (IOP, Bristol, 1994), p. 540.
[7] X. Y. He and L. S. Luo, Phys. Rev. E **55**, R6333 (1997).
[8] P. Asinari and T. Ohwada, Comput. Math. Appl. **58**, 841 (2009).
[9] P. L. Bhatnagar, E. P. Gross, and M. Krook, Phys. Rev. **94**, 511 (1954).
[10] A. Taflove and S. C. Hagness, *Computational Electrodynamics: The Finite-Difference Time-Domain Method*, 2nd ed. (Artech House, Boston, 2000), Vol. xxiii, p. 852.
[11] H. Y. Li and H. Ki, Phys. Rev. E **76**, 066707 (2007).
[12] T. I. Gombosi, *Space Plasma Physics (Lecture Note)* (The University of Michigan, Ann Arbor, 1992).
[13] X. Y. He, X. W. Shan, and G. D. Doolen, Phys. Rev. E **57**, R13 (1998).
[14] T. I. Gombosi, *Gaskinetic Theory* (Cambridge University Press, Cambridge, England, 1994) Vol. xiv, p. 297.
[15] Y. K. Kim and M. E. Rudd, Phys. Rev. A **50**, 3954 (1994).
[16] M. B. Shah *et al.*, J. Phys. B **21**, 2751 (1988).
[17] R. G. Montague, M. F. A. Harrison, and A. C. H. Smith, J. Phys. B **17**, 3295 (1984).
[18] A. J. Kemp, R. E. W. Pfund, and J. Meyer-ter-Vehn, Phys. Plasmas **11**, 5648 (2004).
[19] J. A. Bittencourt, *Fundamentals of Plasma Physics*, 3rd ed. (Springer, New York, 2004), Vol. xxiii, p. 678.
[20] H. Li and H. Ki, J. Phys. A **42**, 155501 (2009).
[21] X. Y. He and L. S. Luo, Phys. Rev. E **56**, 6811 (1997).